



Application of Elastic P-SV Reverse Time Migration to Synthetic Ultrasonic Echo Data from Concrete Members

Maria Grohmann¹ · Ernst Niederleithinger¹ · Stefan Buske² · Christoph Büttner²

Received: 25 October 2022 / Accepted: 15 May 2023
© The Author(s) 2023

Abstract

The ultrasonic echo technique is frequently used in non-destructive testing (NDT) of concrete structures for thickness measurements, geometry determinations as well as localization of built-in components. To improve ultrasonic imaging of complex structures in concrete, we transferred a geophysical imaging technique, the reverse time migration (RTM), to NDT in civil engineering. In contrast to the conventionally used synthetic aperture focusing technique (SAFT) algorithms, RTM is a wave-field continuation method in time and uses the full wave equation. Thus, RTM can handle complicated wave propagations in any direction without dip limitation. In this paper, we focused on the application and evaluation of a two-dimensional (2D) elastic RTM algorithm considering compressional waves, vertically polarized shear waves, and Rayleigh waves. We tested the elastic RTM routine on synthetic ultrasonic echo data generated with a 2D concrete model consisting of several steps and circular air inclusions. As these complex structures can often be found in real-world NDT use cases, their imaging is especially important. By using elastic RTM, we were able to clearly reproduce vertical reflectors and lower edges of circular air voids inside our numerical concrete model. Such structures cannot be imaged with conventional SAFT algorithms. Furthermore, the used elastic RTM approach also yielded a better reconstruction of a horizontal reflector and upper boundaries of circular air inclusions. Our encouraging results demonstrate that elastic RTM has the potential to significantly improve the imaging of complex concrete structures and, thus, is a step forward for detailed, high-quality ultrasonic NDT in civil engineering.

Keywords Concrete structures · Ultrasonic echo technique · Elastic reverse time migration · Synthetic aperture focusing technique

1 Introduction

Quality assurance and damage analysis of concrete structures such as bridges, buildings or highways are essential tasks in civil engineering. Analyzing the interior of new,

repaired or rebuilt concrete structures without damaging them requires non-destructive testing (NDT) methods. A frequently used non-destructive inspection method is the ultrasonic echo technique [1–3]. Important applications include thickness measurements, geometry determinations or the detection of quality issues (cracks, honeycombing, low concrete strength). Another major objective is the localization and characterization of built-in components, in particular post-tensioned tendon ducts [4, 5]. For instance, grouting defects in tendon ducts may decrease the durability of concrete structures [6, 7]. In addition, tendon ducts quite often are not positioned exactly in accordance with construction plans, which can have a significant influence on the structure's load capacity. Thus, the precise localization of these built-in elements is of great importance.

For ultrasonic echo measurements, transmitting and receiving transducers are placed on one side of the concrete specimen. Lightweight dry-coupled point contact transducers are usually used since they can also be utilized on rough

✉ Maria Grohmann
maria.grohmann@bam.de

Ernst Niederleithinger
ernst.niederleithinger@bam.de

Stefan Buske
buske@geophysik.tu-freiberg.de

Christoph Büttner
christoph.buettner@geophysik.tu-freiberg.de

¹ Division Non-Destructive Testing Methods for Civil Engineering, BAM Federal Institute for Materials Research and Testing, Unter den Eichen 87, 12205 Berlin, Germany

² Institute of Geophysics and Geoinformatics, Technical University Bergakademie Freiberg, Gustav Zeuner Str. 12, 09599 Freiberg, Saxony, Germany

surfaces. These transducers have been integrated into commercial products and are available for both, shear (S) waves and compressional (P) waves [8–10]. Currently, for classical NDT tasks on concrete, S-wave transducers, where the direction of oscillation is perpendicular to the plane of incidence (horizontally polarized shear, SH), are predominantly used. SH-waves have the advantage, that they do not convert to other types of waves at any contrast of impedance in two-dimensional (2D) media [11]. Whereas, when using ultrasonic transducers emitting P-waves, mode conversion to vertically polarized shear (SV) waves [12] will occur, as well as the formation of surface waves in form of Rayleigh (R) waves. Thus, using P-wave transducers a more complex wavefield is generated and more scattering effects occur. However, they are used, e.g., for determination of elastic constants [13] or for non-destructive permanent monitoring of concrete [3].

Data processing and imaging of ultrasonic data acquired with transducers is currently mainly done by synthetic aperture focusing technique (SAFT) algorithms [14] operating in time or frequency domain, or by using the closely related Total Focusing Method [15, 16]. In this study, we used the time-domain SAFT algorithm, which is a diffraction stack and creates an image of the investigated specimen by numerically superimposing the reflected signals of single-sided measurements to the imaging points of the reconstructed region. Further details on the SAFT algorithm are described in [17, 18]. A version of the SAFT method using phase evaluation of the measured signal reflections to characterize reflectors has been published by Mayer et al. [19]. The application of SAFT on concrete structures for, e.g., thickness measurements and the detection of defects, such as cracks, delaminations and grouting faults, is presented in numerous studies [8, 17, 20–27]. The localization of objects embedded in concrete structures by using SAFT, as for example tendon ducts, reinforcement and bore holes, has also been successfully explored [5, 8, 17, 20, 21, 23, 27]. However, SAFT suffers from some limitations since only single reflections of the ultrasonic wavefield are taken into account. Thus, artefacts in the reconstructed image occur due to multiple reflections and mode conversions of the wavefield emanating from reflectors inside the concrete specimen. Due to these limitations, it has not been possible to image, for example, vertically or steeply dipping interfaces as well as complex structures such as steps and lower boundaries of voids. Consequently, SAFT does not allow accurate determination of the geometry and dimensions of complicated scattering bodies in concrete. For instance, the location of tendon ducts can be estimated by using SAFT reconstruction, but both the diameter and shape can not be specified accurately.

In exploration seismics, some migration methods have been established for imaging complex structures. Advanced geophysical imaging techniques such as one-way wave equation

imaging were tested on ultrasonic data by Ballier et al. [28] in 2012. Another seismic migration technique called Reverse Time Migration (RTM) is capable to produce even better imaging results of complicated structures. In contrast to SAFT, RTM is a wave-equation based imaging technique. The theory behind RTM is described in detail in Sect. 2.1. RTM was introduced by McMechan [29] and Baysal et al. [30] in 1983 and is now a standard imaging method in the seismic industry. There are RTM algorithms that use the acoustic two-way wave equation (acoustic RTM) as well as routines using the elastic two-way wave equation (elastic RTM) [31]. Farmer et al. [32] demonstrated the usage of acoustic RTM in hydrocarbon exploration by migrating synthetic data from a salt dome model. An acoustic RTM study where real seismic data have been successfully processed for deep targeting and imaging of mineral deposits was published by Ding et al. [33]. In recent years, acoustic RTM has also been applied to ultrasonic data in the field of NDT. In this paper, we focus on related work on the numerical and experimental application of RTM to ultrasonic data acquired on concrete and steel. For example, in the study of Chang et al. [34] acoustic RTM was successfully applied to image a bottom opening crack within a 2D numerical steel model. Zhang et al. [35] used acoustic RTM in the frequency domain to detect numerical and experimental defects in steel after performing higher-order singular value decomposition with the synthetic and real data. Furthermore, in [36], the applicability of acoustic RTM to image synthetic acoustic ultrasonic echo data generated with polyamide- and concrete-like models was proved. Hu et al. [37] demonstrated the application of acoustic RTM on synthetic acoustic ultrasonic data generated with a 2D numerical model of a concrete structure containing an internal fracture. A numerical acoustic RTM study for steel sleeve localization and defect characterization in prefabricated concrete structures is presented by Qi et al. [38]. In the study of Liu et al. [39], an acoustic RTM algorithm combined with travel time tomography is presented for detecting defects in concrete and concrete-filled steel tube columns. Air cavities within three different numerical models could be accurately reconstructed by using the proposed approach. Furthermore, in two previous studies, we successfully applied an acoustic RTM algorithm to real ultrasonic SH-wave data after performing synthetic evaluations [40, 41]. Since SH-waves propagate independently of other wave types, using an acoustic RTM code based on pure P-wave propagation is correct from a kinematical point of view and a valid assumption.¹ The measurement data for our studies were acquired at a concrete foundation slab as well as a polyamide specimen. Compared to SAFT, our acoustic RTM results showed a sig-

¹ For the acoustic RTM evaluations of the real ultrasonic SH-wave data, the acoustic migration velocities corresponded to the shear wave velocities.

nificant improvement in imaging the interior structure of both test specimens. For example, vertical borders inside the foundation slab could be clearly imaged and more features could be found, which was not possible with traditional imaging. Since ultrasonic echo measurements on concrete are performed by exciting elastic waves, the imaging results can be optimized even further with an RTM algorithm that uses the elastic wave equation. Usually, in exploration geophysics, elastic RTM algorithms that evaluate P-, SV- and R-waves (elastic P-SV RTM) are used for imaging seismic data generated by sources emitting P-waves [42–48]. This is due to the fact that P-waves, among other things, arrive first at the receivers, are easily produced by a large number of seismic sources, and can also be used to investigate a marine environment. Therefore, following our successful acoustic RTM applications, our goal was to investigate the potential of using P-wave transducers in combination with elastic P-SV RTM for geometry determination of complex concrete structures. As elastic RTM takes into account the complete wavefield and thus handles various wave effects such as mode-converted waves, it has the potential to improve the imaging of ultrasonic echo data acquired by P-wave transducers compared to classical SAFT reconstruction.

Several studies have been published on the application of elastic RTM to ultrasonic data in NDT of concrete and steel. In the work of Anderson et al. [49] a fully experimental implementation of elastic RTM for the localization of a steel nut glued onto an aluminum plate is presented. Also two debonding locations with insufficient glue could be imaged successfully. Rao et al. [50] explored an elastic least-squares RTM approach for imaging small flaws in numerical heterogeneous structures and a laboratory steel specimen. A synthetic elastic RTM study for detection, localization and size determination of material defects in steel pipes is presented by Nguyen et al. [51]. Mizota et al. [52] published a numerical and experimental elastic RTM research article for non-destructive ultrasonic imaging of numerical and real defects in stainless steel. A further example of the usage of elastic RTM on focused synthetic and experimental ultrasonic data was published in [53]. The authors demonstrated that elastic RTM, combined with a focused ultrasonic P-wavefield, is a promising tool for detecting defects around steel rebars in a concrete object. Nguyen et al. [54] presented a two-step workflow, combining full-waveform inversion and elastic RTM, for reconstruction of a delamination in two numerical concrete models. Another study for the application of elastic RTM on synthetic and measured ultrasonic echo data was published in [55]. The authors were able to inspect the grouting compactness inside two splice sleeves of a precast concrete structure by using elastic RTM. Furthermore, Asadollahi et al. [56] developed an analytical elastic RTM approach to make the RTM algorithm more efficient in terms of memory demand and computation time required.

The authors successfully validated their approach on synthetic ultrasonic echo data generated with a 2D concrete model containing a step as well as a 2D concrete model consisting of a circular air void embedded in a concrete layer. In subsequent work Asadollahi et al. proposed new imaging conditions to damp high-amplitude artefacts and to create more precise amplitudes in elastic RTM images [57]. Recently, Büttner et al. [58] investigated an engineered barrier for nuclear waste storage by applying elastic RTM to synthetic and real ultrasonic echo data. The authors could improve the imaging of deeper parts within the test barrier which consists of salt concrete and contains inclined reflectors.

These studies demonstrate very clearly the advantages of elastic RTM for the imaging quality of measured and synthetic ultrasonic echo data acquired on concrete and steel. The main goal of almost all cited elastic RTM articles was the detection of flaws within the investigated numerical models and real structures. Asadollahi et al. [56], on the other hand, aimed to reconstruct the exact geometries of structural elements inside two numerical concrete models. The objective of our study was also to determine the internal geometry of a 2D numerical concrete model, however it includes much more complex structures. Moreover, the analytical approach presented by Asadollahi et al. [56] focuses on SH-waves and models with back wall structure parallel or inclined to the top edge whereas the elastic RTM routine we used treats the more complex P-SV case and is applicable to arbitrary geometries. The investigated 2D numerical concrete model we used in this study for evaluation of the elastic P-SV RTM algorithm consists of several steps and circular shaped air inclusions. The latter were modeled to represent the usually circular cross-section of tendon ducts. Since internal reflectors and external boundaries of concrete test objects are often inclined or angled, a few steps were defined inside the model. Using this numerical concrete model and a 2D elastic P-SV modeling routine numerous synthetic elastic P-SV data sets were generated. The subsequent application of elastic P-SV RTM and conventional 2D SAFT reconstruction to these synthetic data sets clearly demonstrates that by using elastic P-SV RTM more features inside the numerical concrete model could be detected and the imaging quality could be enhanced significantly. Our results clearly show that the use of P-wave transducers in combination with elastic P-SV RTM has the potential to allow more accurate determination of complex geometries in concrete objects. Hence, elastic P-SV RTM is a step forward for imaging ultrasonic echo data in NDT.

This article is organized as follows: First we explain the RTM algorithm itself (Sect. 2.1). In Sect. 2.2, we present the elastic P-SV modeling routine used. We further demonstrate our numerical concrete model (Sect. 2.3) and the generation of elastic synthetic P-SV data (Sect. 3.1). Section 3.2 and Sect. 3.3 show the application of elastic P-SV RTM

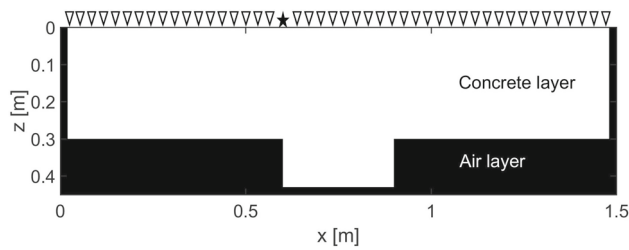


Fig. 1 2D concrete-air model. As an example, the position of shot point No. 28 is marked with a black star and the receiver positions are indicated with triangles

and SAFT reconstruction to the simulated data. Finally, we compare our elastic P-SV RTM results to the reconstruction results obtained using the conventional SAFT imaging method (Sect. 4). The paper ends with a conclusion and an outlook for future work (Sect. 5).

2 Materials and Methods

2.1 Principle of Reverse Time Migration

The RTM technique is a depth migration algorithm that transforms the received signals as a function of recording time into features in subsurface depth. RTM is, in contrast to the conventional used SAFT technique, a wavefield-continuation method in time and uses the full wave equation. It is capable to consider the entire wavefield including multiple reflections. Thus, multi-pathing as well as many other complex situations can be handled. By applying this algorithm, it is possible to image steeply dipping reflectors and structures in areas with strong velocity variations. As a drawback, RTM requires extensive computing power and memory capacity, especially for elastic RTM routines. Nevertheless, RTM has become appealing for the application in the field of NDT due to progress in parallel processing and other computational technologies.

Within the RTM algorithm, two independent simulations of wavefields are performed through predefined models. By applying an imaging condition that combines both wavefields the final RTM image is calculated. Fig. 1 and Fig. 2 schematically show the principle of RTM. For demonstration purposes, we chose a 2D model consisting of a concrete layer surrounded by an air layer and incorporating two vertical reflectors (Fig. 1). Using this model, 71 synthetic shot records, each with 145 traces, were generated for reconstruction with RTM. The shot record for shot point No. 28 is depicted exemplarily in Fig. 2, step 3.

The whole RTM imaging routine can be divided into five steps (Fig. 2). Steps two to four are carried out individually for each source-receiver configuration and are demonstrated here for shot point No. 28.

Step 1: Determination of a suitable velocity and density model including any a priori knowledge. In our demonstration example, we assume the horizontal and maximum vertical extension of the concrete layer to be known, but the shape of the lower boundary to be unknown.

Step 2: The wavefield is calculated forward in time (starting at time zero) from the known source position using a source signal and the specific models from step 1 (source wavefield W_S).

Step 3: The wavefield is simulated backward in time (starting at the maximum recording time) using the estimated models from step 1 and the recorded data (shot record) from measurements or simulations (receiver wavefield W_R). For the backward propagation of the wavefield, the RTM algorithm converts the receivers into sources and the data recorded by the receivers are reversed in time and injected into the sources.

Step 4: This step includes the application of an imaging condition to both wavefields from steps 2 and 3. In this study, we used the imaging condition denoted in equation 1, which is mainly used in the seismic industry. It computes the zero-lag cross-correlation between the source and receiver wavefield W_S and W_R at all model grid points to create an image (cf. [59]):

$$I(x, z) = \int_{t=0}^T W_S(x, z, t) \cdot W_R(x, z, t) dt. \quad (1)$$

$I(x, z)$ denotes the image at point (x, z) and T is the maximum recording time. In the final image, high amplitudes correspond to reflectors in the examined medium.

Step 5: For the final result, the cross-correlation images of all source-receiver configurations are stacked.

2.2 2D Elastic P-SV Finite Difference Modeling Algorithm

The 2D elastic P-SV RTM algorithm we used to perform the migrations is based on a 2D elastic P-SV finite difference modeling algorithm which is included in the Madagascar open source software package [60]. Using the elastic P-SV finite difference code and functions already implemented in Madagascar, we created our own elastic P-SV RTM routine. The 2D elastic finite difference algorithm simulates the P-SV case in the x - z domain (x denotes the horizontal and z the vertical coordinate axis). Therefore, three different wave types are generated after injecting a source signal at $z = 0$ into the model: P-, SV- and R-waves. The particle movement caused by P-waves is in the direction of wave propagation. For SV-waves, the particles vibrate perpendicular to the direction of wave propagation. The particle motion of the high-amplitude R-waves is retrograde elliptical along the direction of travel.

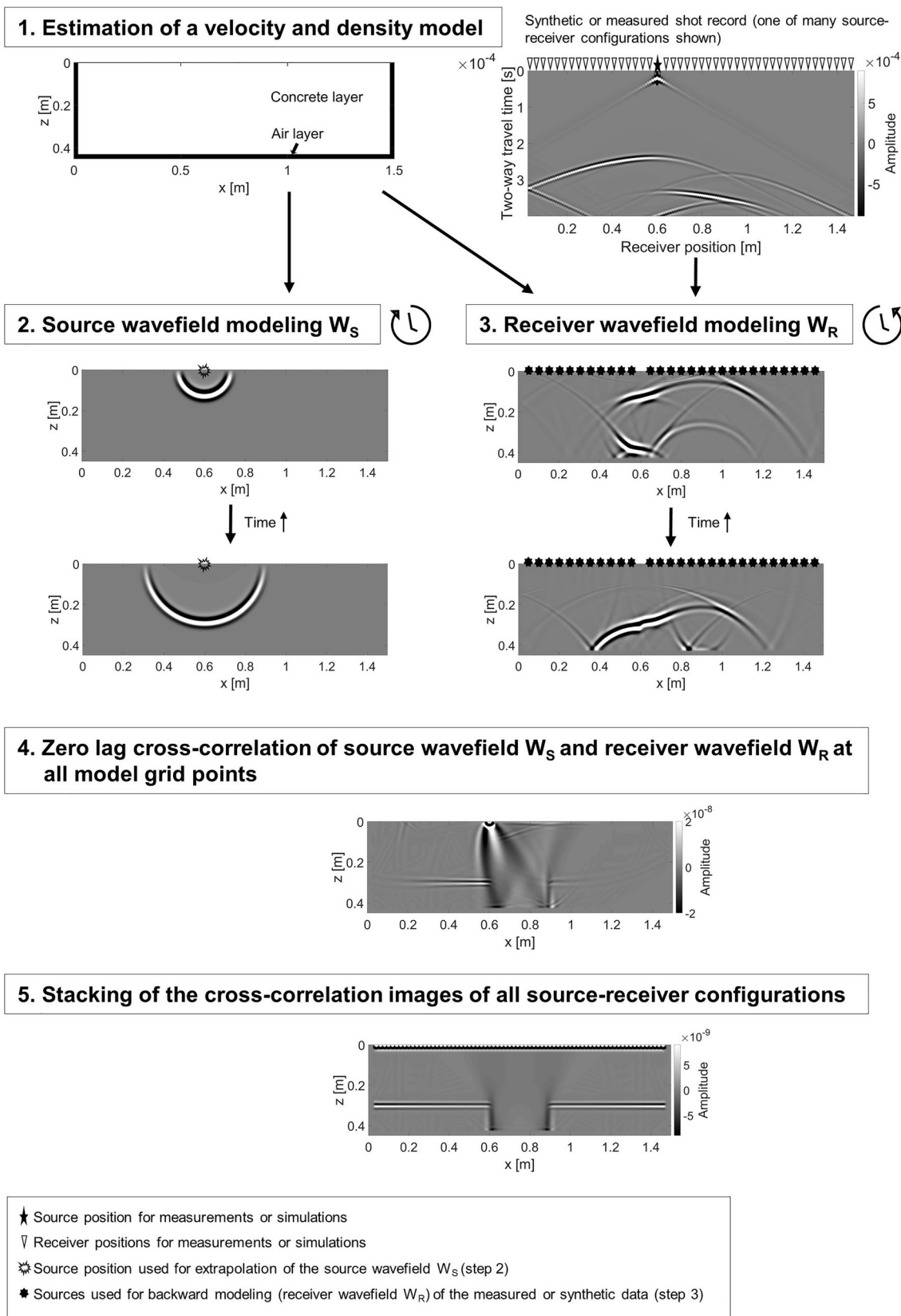


Fig. 2 The Principle of RTM

The 2D elastic P-SV finite difference code operates with a rotated staggered grid (RSG) and is second-order accurate in time and eighth-order accurate in space. Furthermore, the program is parallelized using OpenMP. For our simulations of elastic P-SV wavefields, we assume a 2D medium with homogeneous isotropic materials. Elastic wave propagation in an isotropic medium is calculated within the finite difference modeling routine by solving the following equations and neglecting external forces and boundary conditions:

1. Calculation of the components of the strain tensor ϵ :

$$\begin{aligned} \epsilon_{xx} &= \frac{\partial u_x}{\partial x}, \\ \epsilon_{zz} &= \frac{\partial u_z}{\partial z}, \\ 2\epsilon_{zx} &= \frac{\partial u_z}{\partial x} + \frac{\partial u_x}{\partial z}, \end{aligned} \tag{2}$$

where (x, z) are the 2D spatial coordinates, ϵ_{xx} and ϵ_{zz} are the elongations, and ϵ_{zx} is the shearing. u_x and u_z denote the particle displacement vector wavefields.

2. Calculation of the components of the stress tensor σ :

$$\begin{aligned} \sigma_{xx} &= C_{11}\epsilon_{xx} + C_{13}\epsilon_{zz}, \\ \sigma_{zz} &= C_{33}\epsilon_{zz} + C_{13}\epsilon_{xx}, \\ \sigma_{zx} &= 2C_{55}\epsilon_{zx}, \end{aligned} \tag{3}$$

with: $C_{11} = \lambda + 2\mu$, $C_{33} = \lambda + 2\mu$, $C_{13} = \lambda$, $C_{55} = \mu$,

where σ_{xx} and σ_{zz} denote the two normal stresses and σ_{zx} is the shear stress. C_{11} , C_{13} , C_{33} and C_{55} are elements of the stiffness tensor. λ and μ are the Lamé constants.

3. Calculation of the particle acceleration vector wavefields a_x and a_z :

$$\begin{aligned} a_x &= \frac{1}{\rho} \left(\frac{\sigma_{xx}}{\partial x} + \frac{\sigma_{zx}}{\partial z} \right), \\ a_z &= \frac{1}{\rho} \left(\frac{\sigma_{zx}}{\partial x} + \frac{\sigma_{zz}}{\partial z} \right), \end{aligned} \tag{4}$$

where ρ denotes the density. For modeling the elastic waves with finite differences, the strain tensor ϵ , the stress tensor σ , the vector wavefields $u_{x/z}$, $a_{x/z}$, the density ρ , and the stiffness tensor elements C_{11} , C_{13} , C_{33} and C_{55} have to be discretized on the rotated staggered grid. The equations 2, 3, and 4 describe a system of coupled linear differential equations for the description of the propagation of P-, SV- and R-waves in the x - z plane in an elastic isotropic medium.

4. Performing the time update by the calculation of particle displacement vector wavefields u_x and u_z at time $k + 1$:

$$u_{x_{i,j}/z_{i,j}}^{k+1} = a_{x_{i,j}/z_{i,j}} dt^2 - u_{x_{i,j}/z_{i,j}}^{k-1} + 2u_{x_{i,j}/z_{i,j}}^k, \tag{5}$$

where t is the travel time. i, j and k are the indexes for the x -axis discretization, the z -axis discretization and for the time-axis discretization. dt is the grid step in time. Grid spacing is equal in x - and z -direction. As shown in equation 5, the second time derivatives of u_x and u_z are approximated by central difference quotients of order 2:

$$\frac{\partial^2 u_{x_{i,j}/z_{i,j}}}{\partial t^2} = \frac{u_{x_{i,j}/z_{i,j}}^{k+1} + u_{x_{i,j}/z_{i,j}}^{k-1} - 2u_{x_{i,j}/z_{i,j}}^k}{dt^2}. \tag{6}$$

Compared to the temporal derivatives calculated with the second-order finite difference scheme, the spatial derivatives in 2 and 4 are calculated with eighth-order RSG finite difference schemes. Figure 3 shows the coordinate system of the RSG and the locations where the material parameters or variables are defined or rather calculated. The directions of the spatial derivatives have changed to \tilde{x} and \tilde{z} [61]. The spatial derivatives of u_x and u_z in z - and x -direction in the RSG can be expressed as follows (cf. [61]):

$$\begin{aligned} \frac{\partial}{\partial \tilde{z}} u_{x_{i,j}/z_{i,j}} &\approx \frac{\Delta r}{2\Delta \tilde{z}} \left(\frac{\partial}{\partial \tilde{z}} u_{x_{i,j}/z_{i,j}} - \frac{\partial}{\partial \tilde{x}} u_{x_{i,j}/z_{i,j}} \right), \\ \frac{\partial}{\partial \tilde{x}} u_{x_{i,j}/z_{i,j}} &\approx \frac{\Delta r}{2\Delta \tilde{x}} \left(\frac{\partial}{\partial \tilde{z}} u_{x_{i,j}/z_{i,j}} + \frac{\partial}{\partial \tilde{x}} u_{x_{i,j}/z_{i,j}} \right), \end{aligned} \tag{7}$$

$$\Delta r = \sqrt{\Delta z^2 + \Delta x^2},$$

where Δz and Δx are the lengths of the rectangular cells of the RSG. The spatial derivatives $\frac{\partial}{\partial \tilde{z}}$ and $\frac{\partial}{\partial \tilde{x}}$ of u_x and u_z in \tilde{z} - and \tilde{x} -direction in equation 7 are (cf. [62]):

$$\begin{aligned} \frac{\partial}{\partial \tilde{z}} u_{x_{i,j}/z_{i,j}} &\approx \frac{1}{\Delta r} \sum_{m=1}^M C_m [u_{x/z_{i+(2m-1)/2, j+(2m-1)/2}} \\ &\quad - u_{x/z_{i-(2m-1)/2, j-(2m-1)/2}}], \\ \frac{\partial}{\partial \tilde{x}} u_{x_{i,j}/z_{i,j}} &\approx \frac{1}{\Delta r} \sum_{m=1}^M C_m [u_{x/z_{i+(2m-1)/2, j-(2m-1)/2}} \\ &\quad - u_{x/z_{i-(2m-1)/2, j+(2m-1)/2}}], \end{aligned} \tag{8}$$

where C_m are the coefficients of the $(2M)$ th-order RSG finite difference schemes. Since our elastic routines are eight-order accurate in space, $M = 4$. The C_m ($m=1, 2, 3, 4$) values are calculated by using the following equation [63]:

$$C_m = \frac{(-1)^{m+1}}{2m-1} \prod_{1 \leq n \leq M, n \neq m} \left| \frac{(2n-1)^2}{(2m-1)^2 - (2n-1)^2} \right|. \tag{9}$$

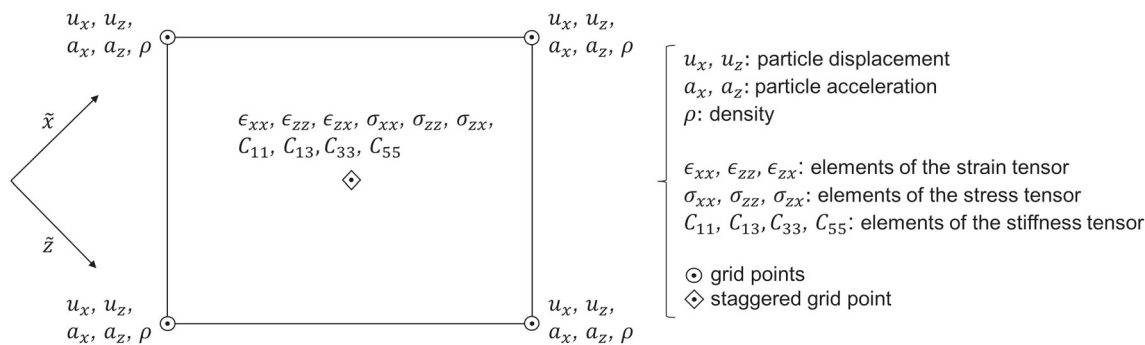


Fig. 3 Elementary cell of the rotated staggered grid (RSG) (based on ([61] Figure 1d)

The application of equation 9 leads to the subsequent values:

C_1	1.1963
C_2	-0.0798
C_3	0.0096
C_4	-6.9754e-04

From equations 7 and 8, it follows for the spatial derivatives $\frac{\partial}{\partial z}$ and $\frac{\partial}{\partial x}$ of u_x and u_z in z - and x -direction:

$$\begin{aligned} \frac{\partial}{\partial z} u_{x_i,j/z_i,j} &\approx \frac{1}{2\Delta z} \sum_{m=1}^M C_m [u_{x/z_{i+(2m-1)/2,j+(2m-1)/2}} \\ &\quad - u_{x/z_{i-(2m-1)/2,j-(2m-1)/2}} \\ &\quad - u_{x/z_{i+(2m-1)/2,j-(2m-1)/2}} + u_{x/z_{i-(2m-1)/2,j+(2m-1)/2}}], \\ \frac{\partial}{\partial x} u_{x_i,j/z_i,j} &\approx \frac{1}{2\Delta x} \sum_{m=1}^M C_m [u_{x/z_{i+(2m-1)/2,j+(2m-1)/2}} \\ &\quad - u_{x/z_{i-(2m-1)/2,j-(2m-1)/2}} + u_{x/z_{i+(2m-1)/2,j-(2m-1)/2}} \\ &\quad - u_{x/z_{i-(2m-1)/2,j+(2m-1)/2}}]. \end{aligned} \tag{10}$$

2.3 Numerical Model and Boundary Conditions

For the generation of the synthetic elastic P-SV ultrasonic data, we defined a 2D numerical concrete model which corresponds in its geometry to one of our laboratory specimens. More details on this specimen can be found in Reinhardt [64]. Our 2D model consists of a three-step homogeneous concrete layer surrounded by a 0.02 m thick layer of air at the sides and lower edge. The model is 2.04 m wide and 0.59 m deep. Four circular air voids with a diameter of 0.08 m are integrated into the concrete layer at different depths. The different thicknesses of the concrete layer as well as the depths of the air voids are shown in Fig. 4. Table 1 summarizes the material parameters used for modeling. We used a density value of 150 kg/m^3 for concrete instead of the correct value of 2400 kg/m^3 . Using the true density value caused instability prob-

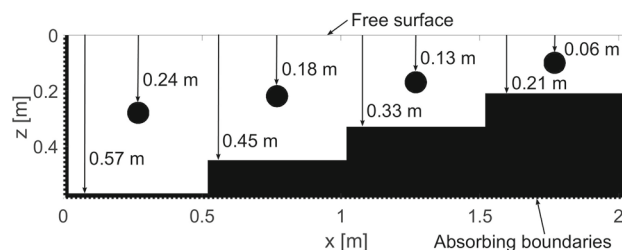


Fig. 4 2D numerical three-step concrete model with absorbing boundaries at the sides and lower edge (marked with a dashed line) and a free surface at the top edge

Table 1 Material parameters used for concrete and air layer

	Concrete	Air
Shear wave velocity $v_s [\frac{m}{s}]$	2750	0
Compressional wave velocity $v_p [\frac{m}{s}]$	4000	333
Density $[\frac{kg}{m^3}]$	150	1.2

lems of the elastic simulations because, the elastic P-SV finite difference algorithm used here does not perform arithmetic averaging of the density, which is essential for stable simulation results at interfaces with large impedance contrasts [65]. By using an elastic P-SV RTM routine available at the Technical University Freiberg, we performed synthetic RTM evaluations on a small numerical concrete-air test model, each with a density value for concrete of 150 kg/m^3 and 2400 kg/m^3 . A comparison of the two elastic P-SV RTM results showed no significant difference in the amplitudes. Hence, using a density value of 150 kg/m^3 for concrete is a valid approximation.

We defined absorbing boundaries at the lateral and lower boundaries of the model domain (marked with a dashed line in Fig. 4). This boundary condition is realized within the elastic P-SV modeling algorithm by the combination of the Clayton and Enquist [66] boundary and the boundary of Cerjan [67]. Furthermore, a free surface was assumed for the top edge of the model space (labelled in Fig. 4) to ensure a total

Table 2 Simulation parameters

Simulation parameter	
Model size [grid points]	4080 (x) x 1180 (z)
Spatial sampling interval [m]	0.0005
Simulation time [s]	0.00085
Temporal sampling interval [s]	$1 \cdot 10^{-8}$
Frequency Ricker wavelet [kHz]	100
Wavelet delay [s]	0.00002

reflection of the wavefield energy. Therefore, the normal and shear stresses above the free surface boundary are set to zero. As source signal for generating elastic synthetic P-SV data and for the source wavefield W_S simulations of the RTM calculations (see Sect. 2.1 step 2), a Ricker wavelet [68, 69] was used. We defined a Ricker wavelet with a time delay of $t_0 = 0.02$ ms and a center frequency of 100 KHz, since our P-wave transducers for real data acquisition on concrete are excited at this frequency.

3 Results

3.1 Simulation of Elastic P-SV Synthetic Ultrasonic Echo Data

As a first step, we generated elastic synthetic P-SV data for imaging with RTM, using the elastic algorithm presented in

Sect. 2.2. Tables 2 and 3 list the corresponding simulation parameters. Using these and the material parameters listed in Table 1, the von Neumann stability criterion for an RSG presented by Saenger et al. [61] is fully satisfied.

Since our ultrasonic measurements usually are conducted from one side of a concrete specimen, we defined 99 point sources and 199 point receivers on the surface of the model. For the elastic P-SV simulations, we injected the source wavelet at the source positions as stress signal into z -direction. The radiation pattern of a stress source corresponds rather to the directivity pattern of the ultrasonic P-wave transducers we use [70]. At the receiver locations the components of the acceleration were read out.

Fig. 5 and Fig. 6 exemplarily show elastic synthetic P-SV data for source position No. 11 located at $x = 0.26$ m above the first air void. The amplitudes of the z - and x -component of acceleration are shown and essential wave events are marked accordingly. For example, the direct R-wave (1) can be clearly seen. Part of the direct R-wave (1) is reflected at the left upper edge of the concrete layer, resulting in an R-wave propagating back along the surface (2) as well as a mode converted bulk wave (3), among others. Furthermore, a head wave (4) guided by the P-wave is formed, which has a weak amplitude. At the first air void, a part of the incident P-wave is reflected as a P-Wave (PP 1) as well as a converted SV-wave (PSV 1). These events are visible in the form of reflection hyperbolas. In addition, the events highlighted with PP 2 and PSV 2 mark the reflected P-wave and the converted SV-wave arising from the P-wave reflection

Table 3 Coordinates of sources and receivers

	Sources	Receivers
Number	99	199
Distance [m]	0.02	0.01
Position of source and receiver No. 1 [m]	$x = 0.04$	$x = 0.03$

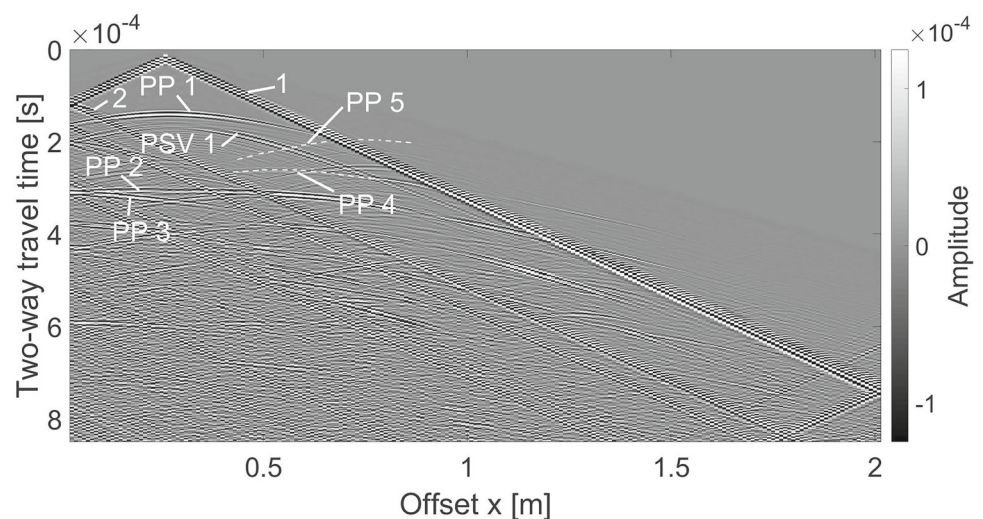
Fig. 5 Elastic P-SV data of shot point No. 11: z -component of acceleration. PSV 1, PP 1, PP 2, PP 3, PP 4, PP 5, 1 and 2 mark essential wave events

Fig. 6 Elastic P-SV data of shot point No. 11: x -component of acceleration. PP 1, PSV 1, PSV 2, PSV 3, PSV 4, PSV 5, 1, 3 and 4 mark essential wave events

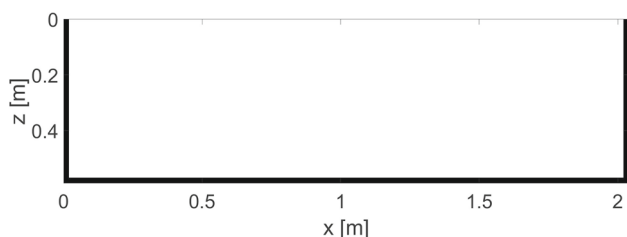
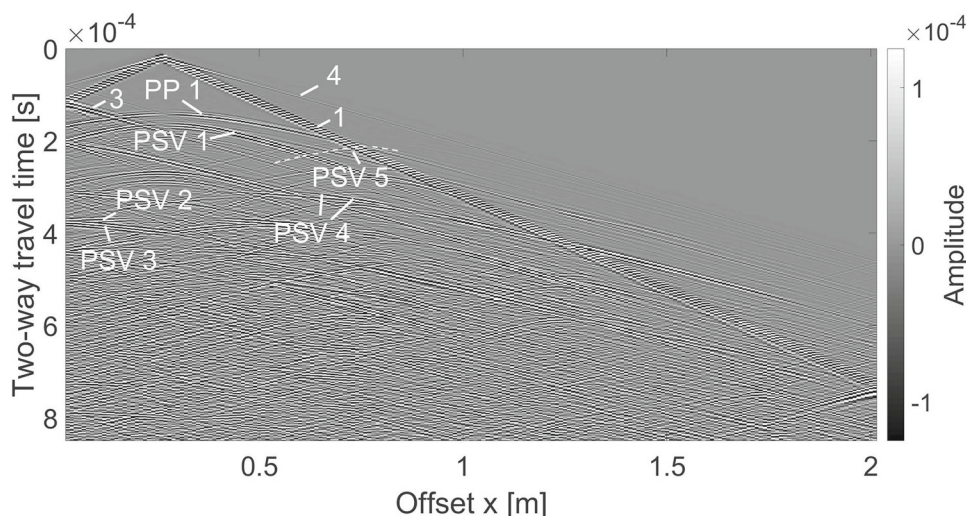


Fig. 7 Structure of the velocity and density models used for the first elastic P-SV RTM

at the lower boundary of the concrete layer. Moreover, the reflected P-wave (PP 3) and converted SV-wave (PSV 3) from P-wave reflection at the lower left edge of the concrete layer are recognizably in the data. Further on, reflection events of the incident P-wave at the corner of the first step can be clearly seen: a reflected P-wave (PP 4) and a mode converted SV-wave (PSV 4). Reflection hyperbolas caused by a reflected P-wave (PP 5) and a converted SV-wave (PSV 5) resulting from P-wave reflection at the second air void are visible with weak amplitudes in the data.

3.2 Elastic P-SV Reverse Time Migration of Synthetic Ultrasonic Echo P-SV Data

The 99 simulated elastic P-SV shot records were evaluated using the elastic P-SV RTM algorithm. Different migration models and the simulation and material parameters from Tables 1, 2 and 3 were used. The final RTM images were generated by computing the zero-lag cross-correlation between the z -components of the source acceleration wavefield W_S and the z -components of the receiver acceleration wavefield W_R as well as by calculating the zero-lag cross-correlation between the x -components of both wavefields.

For the first elastic P-SV RTM evaluation, we assumed the horizontal and maximum vertical extension of the concrete

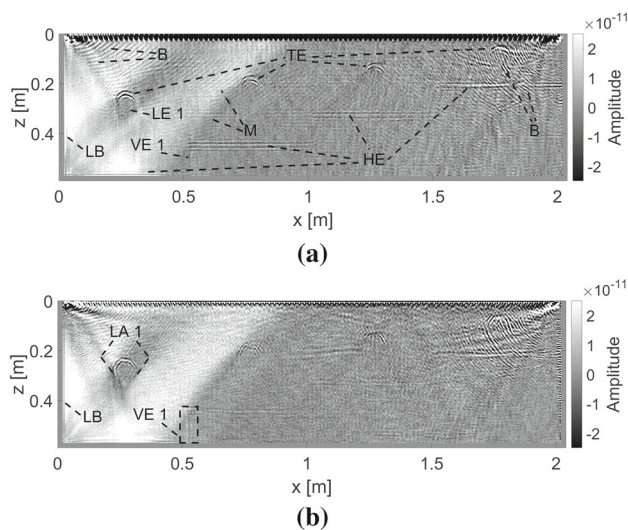


Fig. 8 Elastic P-SV RTM results obtained using the migration model presented in Fig. 7, after (a) cross-correlation of the z -components and after (b) cross-correlation of the x -components (TE: top edges of the four air voids, LE 1: part of the lower edge of the first air void, HE: horizontal edges of the concrete layer, VE 1: vertical edge of the first step, LB: left lateral boundary of the concrete layer, LA 1: lateral edges of the first air void, B and M: migration artefacts (marked exemplarily))

layer to be known (Fig. 7). Hence, the migration model contained no information about internal reflectors. The corresponding elastic P-SV RTM results are shown in Fig. 8. The cross-correlation of the z -components shows the imaging of the top edges of all four air inclusions (marked with TE) as well as the partial mapping of the lower edge of the first air void (marked with LE 1). The vertical edge of the first step is indicated with low amplitude (marked with VE 1). The reconstruction of the horizontal edges of the concrete layer running parallel to the top boundary of the model (marked with HE) was achieved. An apparent double imaging of these horizontal features is visible since the acceleration components of

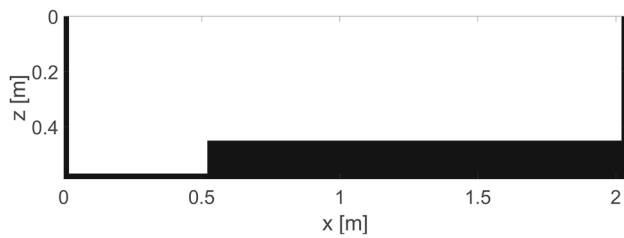


Fig. 9 Structure of the velocity and density models used for the second elastic P-SV RTM

the elastic wavefields were recorded (see for example event PP2 in Fig. 5). Thus, for a correct depth determination of the reflectors, the center between both events has to be assumed. The cross-correlation of the x -components shows the vertical edge of the first step with higher amplitude (dashed rectangle VE 1) and illustrates a better reconstruction of the lateral edges of the first air void (marked with LA 1). The left lateral boundary of the concrete layer is visible in both reconstruction results (marked with LB). The right edge could not be imaged due to the much more complex wavefield arising in the thinnest area of the three-step concrete model.

In the presented RTM results, different migration artefacts caused by unwanted cross-correlations can be observed. For example, cross-correlations of Rayleigh bulk waves can be clearly seen (marked exemplarily with B in Fig. 8a). Migration artefacts due to multiple reflections are visible (marked exemplarily with M in Fig. 8a). Moreover, strong migration artefacts were reproduced in the thickest area of the concrete layer (brighter area), overlapping, for example, the left lateral boundary and the lower concrete edge at $z = 0.57$ m (Fig. 8). These artefacts are considered noise and arise from the correlation of waves that are not accounted for in the cross-correlation imaging condition [40, 41, 71].

With the first elastic P-SV RTM evaluation, we were able to successfully reconstruct the first step. Hence, it was integrated into a next migration model (Fig. 9). The corresponding elastic P-SV RTM results using this one-step model can be seen in Fig. 10. Now the vertical edge of the second step (marked with VE 2) is indicated with low amplitude in the cross-correlation result of the z -components and imaged with higher amplitude in the cross-correlation result of the x -components. Furthermore, with the cross-correlation of the x -components, an improvement of the reconstruction of the first air void (marked with AV 1 in Fig. 10b) could be achieved. Both imaging results show an enhanced mapping of the cross-section of the second air void (marked with AV 2).

For a third elastic P-SV RTM evaluation, the two steps already reconstructed were integrated into a new migration model (Fig. 11). Figure 12 illustrates the corresponding elastic P-SV RTM results. The reconstruction of the cross-section of the third air void (marked with AV 3) was improved and

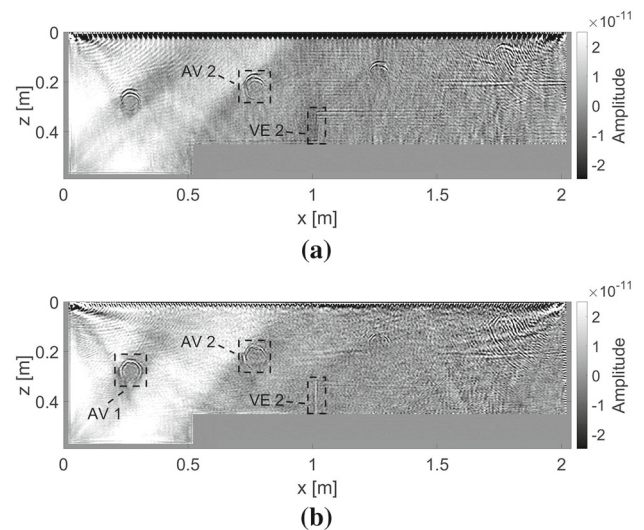


Fig. 10 Elastic P-SV RTM results obtained using the one-step model presented in Fig. 9, after (a) cross-correlation of the z -components and after (b) cross-correlation of the x -components (AV 1: first air void, AV 2: second air void and VE 2: vertical edge of the second step)

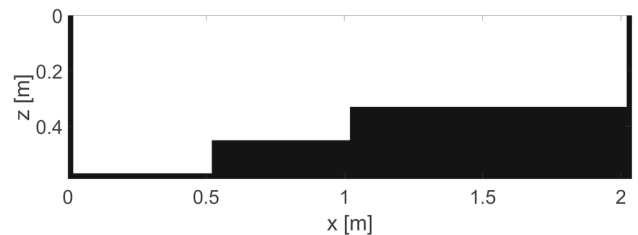


Fig. 11 Structure of the velocity and density models used for the third elastic P-SV RTM

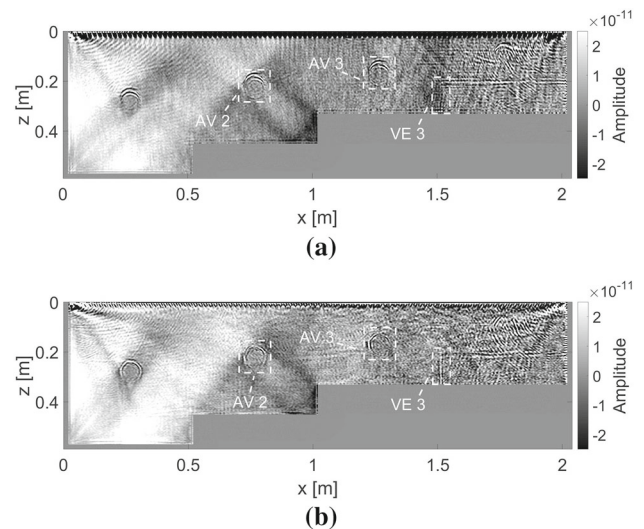


Fig. 12 Elastic P-SV RTM results obtained using the two-step model presented in Fig. 11, after (a) cross-correlation of the z -components and after (b) cross-correlation of the x -components (AV 2: second air void, AV 3: third air void and VE 3: vertical edge of the third step)

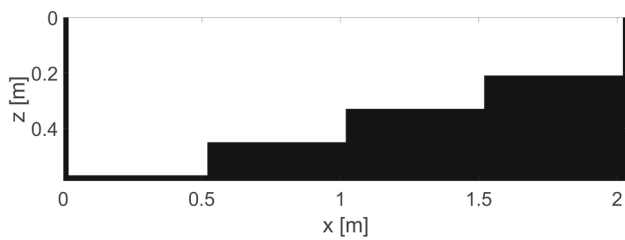


Fig. 13 Structure of the velocity and density models used for the fourth elastic P-SV RTM

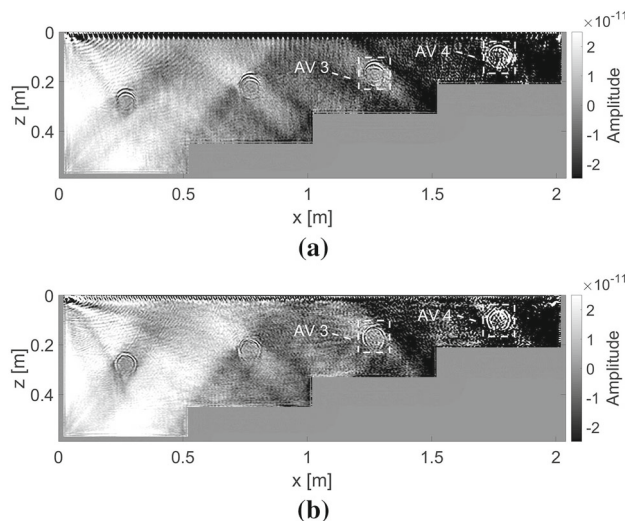


Fig. 14 Elastic P-SV RTM results obtained using the three-step model presented in Fig. 13, after (a) cross-correlation of the z -components and after (b) cross-correlation of the x -components (AV 3: third air void and AV 4: fourth air void)

the imaging of the second air void (marked with AV 2) could also be enhanced. The vertical edge of the third step (marked with VE 3) could be reproduced with the cross-correlation of the x -components and is again indicated with low amplitude in the cross-correlation result of the z -components.

For a final elastic P-SV RTM calculation, all three reconstructed steps were put into a fourth migration model (Fig. 13). Figure 14 shows the cross-correlation results of the z - and x -components. Using the three-step model, the imaging of the fourth air void (marked with AV 4) was achieved and the reconstruction of the third air void (marked with AV 3) could be enhanced.

In the presented elastic RTM results obtained after cross-correlation of the z -components (Fig. 8a, 10a, 12a), the vertical step edges are indicated with weak amplitudes. We were able to improve the mapping of these vertical reflectors by stacking only the migration images of specific shot points. Figure 15 demonstrates the selective stacking result exemplarily for the first RTM evaluation (Fig. 8). Only the migration images of shot points No. 0 to 20 were summed up. Compared to the RTM result presented in Fig. 8a, the vertical

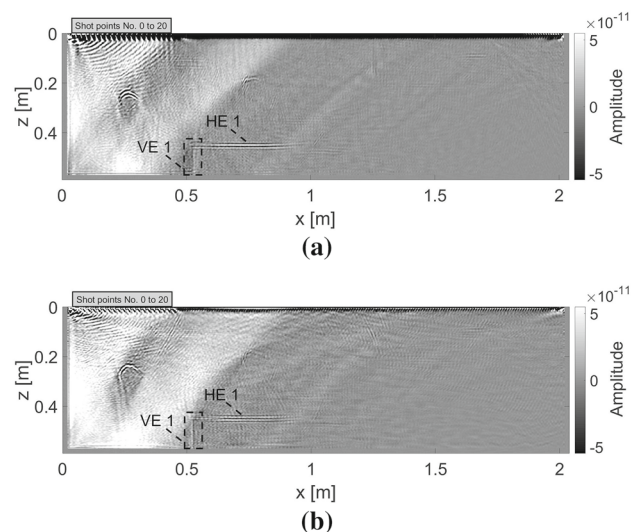


Fig. 15 Elastic P-SV RTM results obtained using the migration model presented in Fig. 7, after (a) cross-correlation of the z -components and after (b) cross-correlation of the x -components. Only the migration images of shot points No. 0 to 20 were stacked. Their locations are indicated by grey boxes (VE 1: vertical edge of the first step and HE 1: horizontal edge of the first step)

step edge (marked with VE 1) is now clearly visible in the cross-correlation result of the z -components. Furthermore, in the cross-correlation result of the x -components, the reconstruction quality of the vertical step edge (marked with VE 1) could be enhanced compared to the RTM result depicted in Fig. 8b. In both RTM images, mapping of the horizontal edge of the first step (marked with HE 1) could be improved as well. Hence, stacking migration images of selected shot points can enhance the imaging of certain reflectors as it minimizes the noise [40, 41].

By applying the elastic RTM algorithm to our 99 synthetic elastic P-SV shot records, we were able to successfully image all reflectors in the model, except for the right edge of the concrete layer. We could show that for complex models like our three-step concrete model, a multi-stage RTM evaluation is necessary to be able to image all reflectors correctly.

3.3 SAFT-Imaging of Synthetic Ultrasonic Echo P-SV Data

Figure 16 shows the reconstruction results obtained by the homogeneous 2D SAFT analysis of the 99 elastic P-SV shot records. We used the Intersaft software [72] to perform the SAFT reconstructions as well as homogeneous velocity models. For a better comparison with the RTM results we presented, it would be more appropriate to perform further SAFT reconstructions with inhomogeneous velocity models containing a priori information. Unfortunately, the latter is not feasible at the moment with the SAFT software available to us.

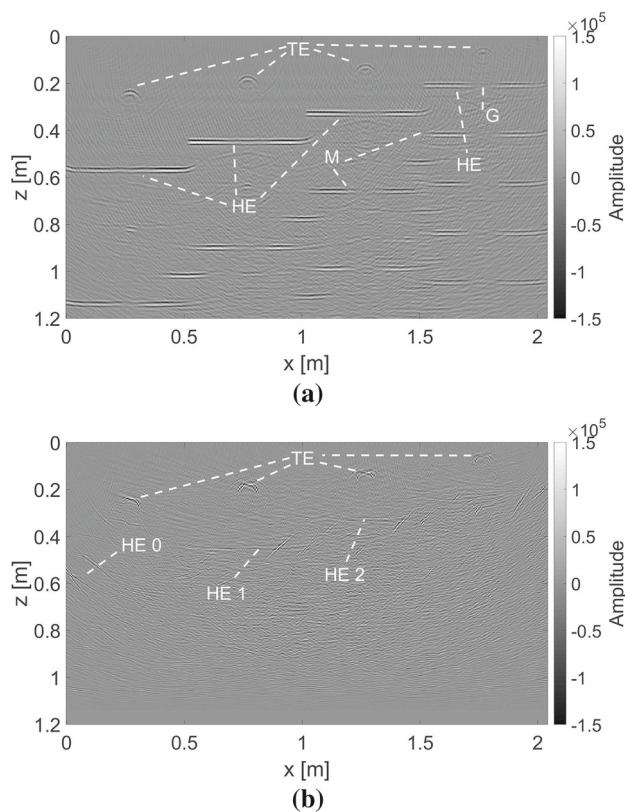


Fig. 16 2D SAFT result of 99 elastic P-SV shot records: (a) SAFT reconstruction of the z -components (HE: horizontal edges of the concrete layer, TE: top edges of the four air voids, M: artifacts due to multiple reflections and G: gap within the lower boundary of the concrete layer) and (b) SAFT reconstruction of the x -components (TE: top edges of the four air voids, HE 0: lower boundary of the concrete layer at $z = 0.57$ m, HE 1: horizontal edge of the first step and HE 2: horizontal edge of the second step)

The z -components of the elastic P-SV data were analyzed using a migration velocity of $v = 4000$ m/s, since P-waves dominate this component of the data due to their directivity. SV-waves, on the other hand, are predominant in the x -component of the data due to their different radiation pattern. Thus, a migration velocity of $v = 2750$ m/s was used for SAFT evaluation of the x -components.

In the obtained SAFT-reconstruction of the z -components (Fig. 16a), the lower boundary of the concrete layer at $z = 0.57$ m and the edges of the steps running parallel to the top edge of the model are clearly visible (marked with HE). Furthermore the top edges of the four air inclusions were imaged successfully (marked with TE). The edge of the third step shows a gap directly below the fourth air void (marked with G) and was not imaged continuously because, a more complex wavefield is generated in this region of the model. Migration artefacts due to multiple reflections in the synthetic data are clearly visible (marked exemplarily with M). In the SAFT result of the x -components (Fig. 16b), the top edges of the air inclusions were imaged (marked with TE). The

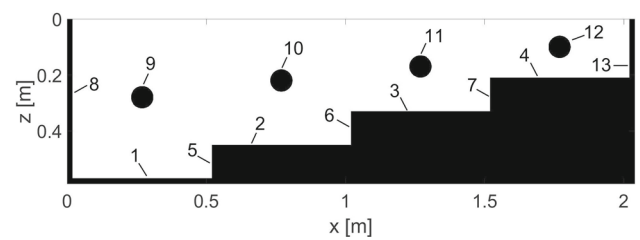


Fig. 17 2D numerical concrete model (structural features are labeled with numbers, which correspond to the numbers in the first column of Table 4)

edges of the first (marked with HE 1) and second (marked with HE 2) step running parallel to the top edge of the model are partially reproduced. The lower boundary of the concrete layer at $z = 0.57$ m (marked with HE 0) is indicated with a weak amplitude.

4 Discussion

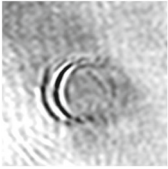
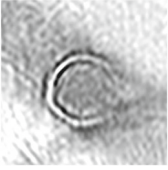
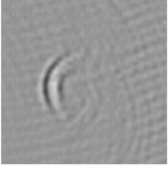
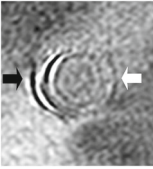
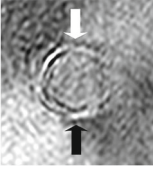
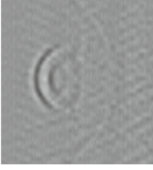
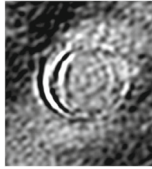
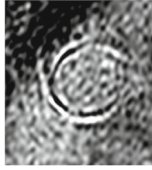

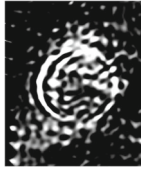
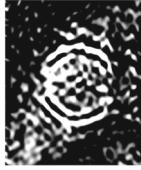

Figure 17 and Table 4 show a summary comparison of reconstructed features of the numerical three-step concrete model (Fig. 4) using elastic P-SV RTM and SAFT. For this purpose, image details from the results shown in Sect. 3.2 and 3.3, which show specific structural elements of the numerical concrete model, are presented in Table 4. Only details from the SAFT result of the z -component are shown, since the SAFT evaluation of the x -component does not map additional reflectors of the numerical model. The numbers in the first column of Table 4 correspond to the numbers in Fig. 17. Comparing elastic P-SV RTM and SAFT, we can see that both algorithms were capable to reproduce the edges of the concrete layer running parallel to the top boundary of the model domain (marked with dashed rectangles: No. 1, No. 2, No. 3 and No. 4). Thereby, in the elastic P-SV RTM results, the edge of the concrete layer at $z = 0.57$ m (No. 1) is overlapped by noise artefacts. It is noticeable that the elastic RTM results of the z -component show a significantly better reconstruction of these horizontal edges compared to the results of the x -component. This phenomenon is caused by the different directivity characteristics of P- and SV-waves. Further on, the third horizontal step edge (No. 4) was mapped more continuously in the elastic RTM result of the z -component than in the SAFT image since the latter shows a clear gap within this horizontal edge.

Elastic P-SV RTM was capable to successfully image the vertical step edges (marked with dashed rectangles: No. 5, No. 6 and No. 7). Imaging of these reflectors was not achieved with SAFT reconstruction. Here, the elastic RTM results of the x -component show a better reconstruction of the vertical edges due to the mentioned different radiation pattern of P- and SV-waves.

Table 4 Comparison of elastic P-SV RTM and SAFT Imaging

Structural Element	Elastic P-SV z-component (Z)	Elastic P-SV x-component (X)	SAFT z-component (S)
1. Horizontal edge at $z = 0.57$ m (taken from: Figs. 8a (Z), Figs. 8b (X) and 16a (S))			
2. Horizontal edge first step (taken from: Figs. 8a (Z), 8b (X) and 16a (S))			
3. Horizontal edge second step (taken from: Figs. 8a (Z), 8b (X) and 16a (S))			
4. Horizontal edge third step (taken from: Figs. 8a (Z), 8b (X) and 16a (S))			
5. Vertical edge first step (taken from: Figs. 8a (Z), 8b (X) and 16a (S))			
6. Vertical edge second step (taken from: Figs. 10a (Z), 10b (X) and 16a (S))			
7. Vertical edge third step (taken from: Figs. 12a (Z), 12b (X) and 16a (S))			
8. Left lateral edge concrete layer (taken from: Figs. 8a (Z), 8b (X) and 16a (S))			

Table 4 continued

Structural Element	Elastic P-SV z-component (Z)	Elastic P-SV x-component (X)	SAFT z-component (S)
9. Cross-section of first air void (taken from: Figs. 14a (Z), 14b (X) and 16a (S))			
10. Cross-section of second air void (taken from: Figs. 14a (Z), 14b (X) and 16a (S))			
11. Cross-section of third air void (taken from: Figs. 14a (Z), 14b (X) and 16a (S))			
12. Cross-section of fourth air void (taken from: Figs. 14a (Z), 14b (X) and 16a (S))			

Imaging of the left lateral edge of the concrete layer (marked with dashed rectangles: No. 8) could be realized by using elastic P-SV RTM, whereas not by using SAFT. However, this boundary is overlaid by strong noise artefacts in the elastic RTM results. For this vertical reflector, elastic RTM of the x -component also provides a better mapping compared to the RTM evaluation of the z -component. The right lateral boundary of the concrete layer could not be reproduced with both imaging algorithms (No. 13 in Fig. 17).

The observation of the four air voids (No. 9, No. 10, No. 11 and No. 12) illustrates that their cross-sections were imaged completely by using elastic RTM whereas by using SAFT only their top edges were reproduced with weak amplitude. Here, the elastic RTM results of the z - and x -component complement each other. Due to the different directional characteristics of P- and SV-waves, the imaging results of the z -component show a better mapping of the top and lower edges of the air inclusions and the imaging results of the x -component illustrate a better reconstruction of the lateral edges (marked exemplarily with arrows for the second air void: No. 10).

It is evident that by using elastic P-SV RTM, imaging of the lower edges of the circular air voids is more difficult than the reconstruction of the other reflectors in the model. The wavefield reflected directly at the lower edges of the air voids, which travels back to the lower edge of the concrete layer and from there back to the receivers, is not visible in most receiver data due to the longer propagation paths. Therefore, the lower edges of the air inclusions are reconstructed from the wavefields diffracted at the lower edges of the air inclusions. The lower edge of the fourth air void was imaged best, since direct reflections at this edge are visible in the receiver data, which is due to the thinner concrete layer and thus the shorter propagation paths. Furthermore, the elastic P-SV RTM results summarized in Table 4 demonstrate that cross-correlation of the x -components gives better horizontal resolution and cross-correlation of the z -components gives better vertical resolution of the searched structural elements. It is therefore reasonable to perform cross-correlations for both acceleration components.

The comparison between the elastic P-SV RTM and SAFT results presented in Table 4 clearly illustrates the limitations of the SAFT algorithm, which is based on the approximate integral solution of the wave equation and normally considers only the shortest wave paths between sources and receivers. Thus, for a concrete test object with strong velocity variations and the associated changes of the wave propagation paths, no optimal migration result can be achieved [73]. Hence, SAFT was not capable to image the lower boundaries of the air inclusions and the vertical features inside our numerical concrete model. RTM, in contrast, directly solves the wave equation and is thus more accurate. All wave effects such as direct and multiple reflections as well as multi-pathing are

taken into account, allowing the imaging of reflectors with inclinations $> 70^\circ$, even in media with strong velocity contrasts. Therefore, reconstruction of the vertical reflectors and lower boundaries of air voids inside our numerical concrete model could be realized successfully. However, since RTM considers all wave types and wave effects, significantly more migration artifacts can be observed in the achieved elastic RTM results compared to the SAFT images.

Despite the mentioned limitations of SAFT in imaging complex structures, a combination of RTM and SAFT could be useful. Depending on the application, the SAFT algorithm could be used for an initial evaluation to correctly determine the position of the lower boundary of a concrete object. This would require fewer RTM evaluations, which are significantly more time and computationally intensive than SAFT analyses. Moreover, SAFT currently has the advantage of being better applicable to real ultrasonic measurements on concrete, because fewer recording transducers per shot are required for a qualitative SAFT result. Our practical experience in ultrasonic RTM measurements on concrete specimens shows that the receivers should be positioned close to each other (1 - 2 cm) in order to generate a meaningful RTM result. Therefore, commercially available ultrasonic systems used mainly for SAFT measurements are not perfectly suited for RTM examinations (as for example A1040 MIRA manufactured by Acoustic Control Systems or Pundit PD8050 produced by Proceq). To realize small receiver spacings for ultrasonic RTM measurements on concrete, we currently use an automated scanner system built at BAM [40, 41] with which transmitting and receiving ultrasonic transducers can be moved automatically. This ultrasonic scanner system has also been successfully used in practice for RTM measurements on a concrete foundation slab [40, 41] and on a prestressed concrete bridge [74]. The ultrasonic echo data acquired in these studies were evaluated by using acoustic RTM algorithms. Furthermore, Büttner et al. [58] investigated successfully an approximately 9 m thick engineered salt concrete barrier for nuclear waste storage with elastic RTM and by using the novel ultrasonic measuring system LAUS (Large Aperture Ultrasonic System) [75]. In order to achieve a sufficient penetration depth, a lower excitation frequency of the S-wave transducers (25 kHz) than usual was used, and the usage of large distances between recording transducers (11 cm) yielded good quality RTM results. These RTM studies show that RTM is applicable not only to simulated but also to real ultrasonic measurements on concrete.

5 Conclusions and Future Work

In this paper, the applicability of a 2D elastic P-SV RTM algorithm to image ultrasonic echo data generated by P-wave

transducers was evaluated based on synthetic data. To this end, 99 elastic shot records were simulated with a complex numerical concrete model containing three steps and four circular air voids. Our results show that, in comparison to SAFT imaging, elastic P-SV RTM is a step forward for ultrasonic NDT of challenging concrete structures. Specifically, vertical borders could be imaged clearly as well as lower edges of circular air voids. This would not have been possible with traditional SAFT imaging. Moreover, reconstruction of the lower boundary of the concrete layer in the thinnest part of the model at $z = 0.21$ m as well as imaging of the top edges of the four air inclusions could be improved.

Motivated by our promising results, there are several aspects we would like to address in future work. Our synthetic elastic RTM results indicate, that the usage of real ultrasonic P-wave transducers in combination with elastic P-SV RTM imaging has the potential to correctly reconstruct complicated structures in real concrete objects. Hence, the applicability of our 2D elastic P-SV RTM algorithm to image measured ultrasonic echo data has to be evaluated. For appropriate reconstruction of complex reflectors, both z - and x -components of the ultrasonic wavefield must be recorded by transducers due to their respective advantages shown. Corresponding ultrasonic echo measurements are currently being performed at one of our laboratory concrete specimens, whose geometry is similar to the numerical model presented in this paper.

For better imaging of the lower boundaries of the air voids, RTM artefacts have to be analyzed and eliminated. For this task alternatives to the cross-correlation imaging condition may be applied. Moreover, for elastic RTM reconstruction of SH-wave ultrasonic echo data, the potential of an 2D elastic SH-code has to be evaluated and compared to our elastic P-SV results. Therefore, we are currently modifying the elastic P-SV code to an elastic SH routine, so that SH-waves can be modeled two-dimensionally in the x - z plane.

A disadvantage of elastic RTM compared to SAFT is that the reconstructions are computationally intensive. Thus, a more efficient calculation of elastic RTM reconstructions by using graphics processing units (GPU) instead of conventional central processing units (CPU) is targeted in order to minimize the computing capacities. The use of powerful GPUs can tremendously speed up the finite difference calculations of the elastic wavefields and minimize the memory requirements [76].

Acknowledgements Many thanks to our colleagues at BAM 8.2, especially Vera Lay and Stefan Maack. Big thanks also goes to our colleagues in the IT department for supporting the computationally intensive elastic Reverse Time Migration (RTM) calculations. Klaus Mayer from the University of Kassel (Germany) implemented the SAFT algorithm for the reconstruction of our synthetic ultrasonic data. We thank him for providing the algorithm and fruitful discussions.

Funding Open Access funding enabled and organized by Projekt DEAL. No funding was received for conducting this study.

Data available Data are available from the corresponding author upon request.

Open Access This article is licensed under a Creative Commons Attribution 4.0 International License, which permits use, sharing, adaptation, distribution and reproduction in any medium or format, as long as you give appropriate credit to the original author(s) and the source, provide a link to the Creative Commons licence, and indicate if changes were made. The images or other third party material in this article are included in the article's Creative Commons licence, unless indicated otherwise in a credit line to the material. If material is not included in the article's Creative Commons licence and your intended use is not permitted by statutory regulation or exceeds the permitted use, you will need to obtain permission directly from the copyright holder. To view a copy of this licence, visit <http://creativecommons.org/licenses/by/4.0/>.

References

- Schickert, M., Krause, M.: Ultrasonic techniques for evaluation of reinforced concrete structures. In: Maierhofer, C., Reinhardt, H.-W., Dobmann, G. (eds.) *Non-destructive Evaluation of Reinforced Concrete Structures*, vol. 2, pp. 490–530. Woodhead Publishing Limited, Sawston, Great Britain (2010). <https://doi.org/10.1533/9781845699604.2.490>
- Krause, M.: Localization of grouting faults in post tensioned concrete structure. In: Breyse, D. (ed.) *Non-Destructive Assessment of Concrete Structures: Reliability and Limits of Single and Combined Techniques*, pp. 263–304. Springer, Berlin, Germany (2012). https://doi.org/10.1007/978-94-007-2736-6_6
- Niederleithinger, E., Wolf, J., Mielentz, F., Wiggenhauser, H., Pirsakawetz, S.: Embedded ultrasonic transducers for active and passive concrete monitoring. *Sensors* **15**(5), 9756–9772 (2015). <https://doi.org/10.3390/s150509756>
- Krause, M., Milmann, B., Schickert, M., K.M.: Investigation of Tendon Ducts by Means of Ultrasonic Echo Methods: A Comparative Study. Paper presented at the European Conference on NDT, Berlin (2006)
- Krause, M., Mayer, K., Friese, M., Milmann, B., Mielentz, F., Ballier, G.: Progress in ultrasonic tendon duct imaging. *Eur. J. Environ. Civil Eng.* (2011). <https://doi.org/10.1080/19648189.2011.9693341>
- Eichinger, E.M., Diem, J., J., K.: Bewertung des Zustandes von Spanngliedern auf der Grundlage von Untersuchungen an Massivbrücken der Stadt Wien. *Institut für Stahlbeton und Massivbau* (1) (2000)
- Vogel, T.: Zustandserfassung von Brücken bei deren Abbruch - Erkenntnisse für Neubau und Erhaltung. *Bauingenieur* **77**(12), 559–567 (2002)
- Friese, M., Wiggenhauser, H.: New NDT technique for concrete structures: ultrasonic linear array and advanced imaging techniques. In: *Proceedings of NDE/NDT for Highways and Bridges, Structural Materials Technology (SMT)*, Oakland (2008)
- Bishko, A.V., Samokrutov, A.A., Shevaldykin, V.G.: Ultrasonic echo-pulse tomography of concrete using shear waves low-frequency phased antenna arrays. In: *Proceedings of 17th World Conference on Nondestructive Testing*, Shanghai, China (2008)
- Shevaldykin, V.G., Samokrutov, A.A., Kozlov, V.N.: Ultrasonic low-frequency short-pulse transducers with dry point contact: development and application. In: *Proceedings of International Symposium, NDT-CE*, Berlin, Germany (2003)

11. Shull, P.J. (ed.): *Nondestructive Evaluation: Theory, Techniques and Applications*. Dekker, M., New York (2002). <https://doi.org/10.1201/9780203911068>
12. Knödel, K., Krummel, H., Lange, G. (eds.): *Handbuch zur Erkundung des Untergrundes Von Deponien: Band 3: Geophysik*. Springer, Berlin (2005)
13. Rentsch, W., Krompholz, G.: Zur Bestimmung elastischer Konstanten durch Schallgeschwindigkeitsmessungen. *Zeitschrift für Bergbau, Hüttenwesen und verwandte Wissenschaften* **13**, 492–504 (1961)
14. Unterausschuss Ultraschallprüfung FA ZfP im Bauwesen: Merkblatt B 04 Ultraschallverfahren zur Zerstörungsfreien Prüfung im Bauwesen. Deutsche Gesellschaft für Zerstörungsfreie Prüfung DGZfP (2018)
15. Holmes, C., Drinkwater, B.W., Wilcox, P.D.: Post-processing of the full matrix of ultrasonic transmit-receive array data for non-destructive evaluation. *NDT & e International* **38**(8), 701–711 (2005). <https://doi.org/10.1016/j.ndteint.2005.04.002>
16. Kuchipudi, S.T., Ghosh, D.: An ultrasonic wave-based framework for imaging internal cracks in concrete. *Struct. Control Health Monit.* **29**(12), 3108 (2022). <https://doi.org/10.1002/stc.3108>
17. Schickert, M., Krause, M., Müller, W.: Ultrasonic imaging of concrete elements using reconstruction by synthetic aperture focusing technique. *J. Mater. Civil Eng.* **15**, 235–246 (2003). [https://doi.org/10.1061/\(ASCE\)0899-1561\(2003\)15:3\(235\)](https://doi.org/10.1061/(ASCE)0899-1561(2003)15:3(235))
18. Mayer, K., Marklein, R., Langenberg, K.-J., Kreutter, T.: Three-dimensional imaging system based on Fourier transform synthetic aperture focusing technique. *Ultrasonics* **28**(4), 241–255 (1990). [https://doi.org/10.1016/0041-624X\(90\)90091-2](https://doi.org/10.1016/0041-624X(90)90091-2)
19. Mayer, K., Langenberg, K.-J., Krause, M., Milmann, B., Mielentz, F.: Characterization of reflector types by phase-sensitive ultrasonic data processing and imaging. *J. Nondestruct. Eval.* **27**(1), 35–45 (2008). <https://doi.org/10.1007/s10921-008-0035-3>
20. Choi, H., Bittner, J., Popovics, J.S.: Comparison of ultrasonic imaging techniques for full-scale reinforced concrete. *Transp. Res. Rec.* **2592**(1), 126–135 (2016). <https://doi.org/10.3141/2592-14>
21. Hoegh, K., Khazanovich, L.: Extended synthetic aperture focusing technique for ultrasonic imaging of concrete. *NDT & E Int.* **74**, 33–42 (2015). <https://doi.org/10.1016/j.ndteint.2015.05.001>
22. Shokouhi, P., Wolf, J., Wiggenshauser, H.: Detection of delamination in concrete bridge decks by joint amplitude and phase analysis of ultrasonic array measurements. *J. Bridge Eng.* **19**(3), 04013005 (2014). [https://doi.org/10.1061/\(ASCE\)BE.1943-5592.0000513](https://doi.org/10.1061/(ASCE)BE.1943-5592.0000513)
23. Lay, V., Effner, U., Niederleithinger, E., Arendt, J., Hofmann, M., Kudla, W.: Ultrasonic quality assurance at magnesia shotcrete sealing structures. *Sensors* **22**(22), 8717 (2022). <https://doi.org/10.3390/s22228717>
24. Ghosh, D., Kumar, R., Ganguli, A., Mukherjee, A.: Nondestructive evaluation of rebar corrosion-induced damage in concrete through ultrasonic imaging. *J. Mater. Civ. Eng.* **32**(10), 04020294 (2020). [https://doi.org/10.1061/\(ASCE\)MT.1943-5533.0003398](https://doi.org/10.1061/(ASCE)MT.1943-5533.0003398)
25. Beniwal, S., Ganguli, A.: Localized condition monitoring around rebars using focused ultrasonic field and SAFT. *Res. Nondestruct. Eval.* **27**(1), 48–67 (2016)
26. Effner, U., Mielentz, F., Niederleithinger, E., Friedrich, C., Mauke, R., Mayer, K.: Testing repository engineered barrier systems for cracks—a challenge. *Materialwissenschaft und Werkstofftechnik* **52**(1), 19–31 (2021). <https://doi.org/10.1002/mawe.202000118>
27. Krause, M., Milmann, B., Mielentz, F., Streicher, D., Redmer, B., Mayer, K., Langenberg, K.-J., Schickert, M.: Ultrasonic imaging methods for investigation of post-tensioned concrete structures: a study of interfaces at artificial grouting faults and its verification. *J. Nondestruct. Eval.* **27**, 67–82 (2008). <https://doi.org/10.1007/s10921-008-0033-5>
28. Ballier, G., Mayer, K., Langenberg, K.-J., Schulze, S., Krause, M.: Improvements on tendon duct examination by modelling and imaging with synthetic aperture and one-way inverse methods. In: *Proceedings of 18th World Conference on Nondestructive Testing*, Durban, South Africa (2012)
29. McMechan, G.A.: Migration by extrapolation of time-dependent boundary values. *Geophys. Prospect.* **31**(3), 413–420 (1983). <https://doi.org/10.1111/j.1365-2478.1983.tb01060.x>
30. Baysal, E., Kosloff, D.D., Sherwood, J.W.C.: Reverse time migration. *Geophysics* **48**(11), 1514–1524 (1983). <https://doi.org/10.1190/1.1441434>
31. Zhou, H., Hu, H., Zou, Z., Wo, Y., Youn, O.: Reverse time migration: a prospect of seismic imaging methodology. *Earth Sci. Rev.* **179**, 207–227 (2018). <https://doi.org/10.1016/j.earscirev.2018.02.008>
32. Farmer, P.A., Jones, I.F., Zhou, H., Bloor, R.I., Goodwin, M.C.: Application of reverse time migration to complex imaging problems. *First Break* **24**(9), 65–73 (2006). <https://doi.org/10.3997/1365-2397.24.9.27105>
33. Ding, Y., Malehmir, A.: Reverse time migration (RTM) imaging of iron oxide deposits in the Ludvika mining area. *Sweden Solid Earth* **12**(8), 1707–1718 (2021). <https://doi.org/10.5194/se-12-1707-2021>
34. Chang, J., Wang, C., Tang, Y., Li, W.: Numerical investigations of ultrasonic reverse time migration for complex cracks near the surface. *IEEE Access* **10**, 5559–5567 (2022). <https://doi.org/10.1109/ACCESS.2021.3140119>
35. Zhang, Y., Gao, X., Zhang, J., Jiao, J.: An ultrasonic reverse time migration imaging method based on higher-order singular value decomposition. *Sensors* **22**(7), 2534 (2022). <https://doi.org/10.3390/s22072534>
36. Müller, S., Niederleithinger, E., Bohlen, T.: Reverse time migration: a seismic imaging technique applied to synthetic ultrasonic data. *Int. J. Geophys.* (2012). <https://doi.org/10.1155/2012/128465>
37. Hu, M., Chen, S., Pan, D.: Reverse time migration based ultrasonic wave detection for concrete structures. In: *Proceedings of Design, Construction and Maintenance of Bridges: Geo-Hubei International Conference on Sustainable Infrastructure*, pp. 53–60 (2014)
38. Qi, Y., Chen, Z., Liu, H., Qi, Y., Tong, H., Xie, J.: Ultrasonic inspection of prefabricated constructions using reverse time migration imaging method. In: *2019 IEEE International Conference on Signal, Information and Data Processing (ICSIDP)*, pp. 1–4 (2019). <https://doi.org/10.1109/ICSIDP47821.2019.9172817>
39. Liu, H., Xia, H., Zhuang, M., Long, Z., Liu, C., Cui, J., Xu, B., Hu, Q., Liu, Q.: Reverse time migration of acoustic waves for imaging based defects detection for concrete and CFST structures. *Mech. Syst. Signal Process.* **117**, 210–220 (2019). <https://doi.org/10.1016/j.ymsp.2018.07.011>
40. Grohmann, M., Niederleithinger, E., Buske, S.: Geometry determination of a foundation slab using the ultrasonic echo technique and geophysical migration methods. *J. Nondestruct. Eval.* (2016). <https://doi.org/10.1007/s10921-016-0334-z>
41. Grohmann, M., Müller, S., Niederleithinger, E., Sieber, S.: Reverse time migration: introducing a new imaging technique for ultrasonic measurements in civil engineering. *Near Surf. Geophys.* **15**(3), 242–258 (2017). <https://doi.org/10.3997/1873-0604.2017006>
42. Chen, T., Huang, L.: Imaging faults using elastic reverse-time migration with updated velocities of waveform inversion. *GRC Trans.* **37** (2013)
43. Rocha, D., Sava, P.: Elastic least-squares reverse time migration using the energy norm. *Geophysics* **83**(3), 237–248 (2018). <https://doi.org/10.1190/geo2017-0465.1>
44. Yan, H., Yang, L., Dai, H., Li, X.-Y.: Implementation of elastic prestack reverse-time migration using an efficient dinite-difference scheme. *Acta Geophys.* **64**(5), 1605–1625 (2016). <https://doi.org/10.1515/acgeo-2016-0078>

45. Zhong, Y., Gu, H., Liu, Y., Mao, Q.: Elastic reverse-time migration with complex topography. *Energies* (2021). <https://doi.org/10.3390/en14237837>
46. Xiao, X., Leaney, W.S.: Local vertical seismic profiling (VSP) elastic reverse-time migration and migration resolution: salt-flank imaging with transmitted P-to-S waves. *Geophysics* **75**(2), 35–49 (2010). <https://doi.org/10.1190/1.3309460>
47. Shi, Y., Zhang, W., Wang, Y.: Seismic elastic RTM with vector-wavefield decomposition. *J. Geophys. Eng.* **16**(3), 509–524 (2019). <https://doi.org/10.1093/jge/gxz023>
48. Jing, C., Singh, V.P., Custodio, D., Cha, Y.H., Ross, W.S.: Benefits and applications of elastic reverse time migration in salt-related imaging. Expanded Abstract, Society of Exploration Geophysicists International Exposition and 87th Annual Meeting, 2017 (2017). <https://doi.org/10.1190/segam2017-17409572.1>
49. Anderson, B.E., Griffa, M., Bas, P.-Y.L., Ulrich, T.J., Johnson, P.A.: Experimental implementation of reverse time migration for nondestructive evaluation applications. *J. Acoust. Soc. Am.* **129**(1), 8–14 (2011). <https://doi.org/10.1121/1.3526379>
50. Rao, J., Yang, J., He, J., Huang, M., Rank, E.: Elastic least-squares reverse-time migration with density variation for flaw imaging in heterogeneous structures. *Smart Mater. Struct.* **29**(3), 035017 (2020). <https://doi.org/10.1088/1361-665X/ab6ba4>
51. Nguyen, L.T., Kocur, G.K., Saenger, E.H.: Defect mapping in pipes by ultrasonic wavefield cross-correlation: a synthetic verification. *Ultrasonics* **90**, 153–165 (2018). <https://doi.org/10.1016/j.ultras.2018.06.014>
52. Mizota, H., Amano, Y., Nakahata, K.: Application of the reverse time migration method to ultrasonic nondestructive imaging for anisotropic materials. *Mater. Eval.* **80**(7), 28–37 (2022). <https://doi.org/10.32548/2022.me-04244>
53. Beniwal, S., Ganguli, A.: Defect detection around rebars in concrete using focused ultrasound and reverse time migration. *Ultrasonics* **62**, 112–125 (2015). <https://doi.org/10.1016/j.ultras.2015.05.008>
54. Nguyen, L.T., Modrak, R.T.: Ultrasonic wavefield inversion and migration in complex heterogeneous structures: 2d numerical imaging and nondestructive testing experiments. *Ultrasonics* **82**, 357–370 (2018). <https://doi.org/10.1016/j.ultras.2017.09.011>
55. Liu, H., Qi, Y., Chen, Z., Tong, H., Liu, C., Zhuang, M.: Ultrasonic inspection of grouted splice sleeves in precast concrete structures using elastic reverse time migration method. *Mech. Syst. Signal Process.* **148**, 107152 (2021). <https://doi.org/10.1016/j.ymsp.2020.107152>
56. Asadollahi, A., Khazanovich, L.: Analytical reverse time migration: an innovation in imaging of infrastructures using ultrasonic shear waves. *Ultrasonics* **88**, 185–192 (2018). <https://doi.org/10.1016/j.ultras.2018.04.005>
57. Asadollahi, A., Khazanovich, L.: Analytical reverse time migration with new imaging conditions for one-sided nondestructive evaluation of concrete elements using shear waves. *Ultrasonics* **99**, 105960 (2019). <https://doi.org/10.1016/j.ultras.2019.105960>
58. Büttner, C., Niederleithinger, E., Buske, S., Friedrich, C.: Ultrasonic echo localization using seismic migration techniques in engineered barriers for nuclear waste storage. *J. Nondestruct. Eval.* **40**(4), 1–10 (2021). <https://doi.org/10.1007/s10921-021-00824-3>
59. Sava, P., Hill, S.J.: Overview and classification of wavefield seismic imaging methods. *Lead. Edge* **28**(2), 170–183 (2009). <https://doi.org/10.1190/1.3086052>
60. Fomel, S., Sava, P., Vlad, I., Liu, Y., Bashkardin, V.: Madagascar: open-source software project for multidimensional data analysis and reproducible computational experiments. *J. Open Res. Softw.* (2013). <https://doi.org/10.5334/jors.ag>
61. Saenger, E.H., Gold, N., Shapiro, S.A.: Modeling the propagation of elastic waves using a modified finite-difference grid. *Wave Motion* **31**(1), 77–92 (2000). [https://doi.org/10.1016/S0165-2125\(99\)00023-2](https://doi.org/10.1016/S0165-2125(99)00023-2)
62. Yang, L., Yan, H., Liu, H.: Optimal rotated staggered-grid finite-difference schemes for elastic wave modeling in TTI media. *J. Appl. Geophys.* **122**, 40–52 (2015). <https://doi.org/10.1016/j.jappgeo.2015.08.007>
63. Liu, Y., Sen, M.K.: An implicit staggered-grid finite-difference method for seismic modelling. *Geophys. J. Int.* **179**(1), 459–474 (2009). <https://doi.org/10.1111/j.1365-246X.2009.04305.x>
64. Reinhardt, H.W.: Zerstörungsfreie Strukturbestimmung von Betonbauteilen mit akustischen und elektromagnetischen Echo-Verfahren: Abschlussbericht Forschergruppe FOR384. Liste der erstellten Prüfkörper, Anhang (2007)
65. Bohlen, T., Saenger, E.H.: Accuracy of heterogeneous staggered-grid finite-difference modeling of Rayleigh waves. *Geophysics* **71**(4), 109–115 (2006). <https://doi.org/10.1190/1.2213051>
66. Clayton, R., Engquist, B.: Absorbing boundary conditions for acoustic and elastic wave equations. *Bull. Seismol. Soc. Am.* **67**(6), 1529–1540 (1977). <https://doi.org/10.1785/BSSA0670061529>
67. Cerjan, C., Kosloff, D., Kosloff, R., Reshef, M.: A nonreflecting boundary condition for discrete acoustic and elastic wave equations. *Geophysics* **50**(4), 705–708 (1985). <https://doi.org/10.1190/1.1441945>
68. Ricker, N.: The form and laws of propagation of seismic wavelets. *Geophysics* (1953). <https://doi.org/10.1190/1.1437843>
69. Gholamy, A., Kreinovich, V.: Why Ricker wavelets are successful in processing seismic data: Towards a theoretical explanation. Paper presented at IEEE Symposium on Computational Intelligence for Engineering Solutions (CIES), Orlando Florida, USA (2014). <https://doi.org/10.1109/CIES.2014.7011824>
70. Maack, S.: Untersuchungen zum Schallfeld niederfrequenter Ultraschallprüfköpfe für die Anwendung im Bauwesen. PhD thesis, Bundesanstalt für Materialforschung und -prüfung (BAM) (2012)
71. Díaz, E., Sava, P.: Understanding the reverse time migration backscattering: noise or signal? *Geophys. Prospect.* **64**(3), 581–594 (2016). <https://doi.org/10.1111/1365-2478.12232>
72. Mayer, K., Cinta, P.M.: User Guide of Graphical User Interface inter_unity. Department of Computational Electronics and Photonics, University of Kassel, Kassel (2012)
73. Geoltrain, S., Brac, J.: Can we image complex structures with first-arrival traveltimes? *Geophysics* **58**(4), 564–575 (1993). <https://doi.org/10.1190/1.1443439>
74. Müller, S.: Weiterentwicklung der Reverse Time Migration zur Anwendung auf Ultraschall-Echo-Daten in der zerstörungsfreien Prüfung. PhD thesis, Bundesanstalt für Materialforschung und -prüfung (BAM), Submitted at RWTH Aachen University (2023)
75. Wiggenhauser, H., Niederleithinger, E., Milmann, B.: Zerstörungsfreie Ultraschallprüfung dicker und hochbewehrter Betonbauteile. *Bautechnik* **94**(10), 682–688 (2017). <https://doi.org/10.1002/bate.201700040>
76. Weiss, R.M., Shragge, J.: Solving 3D anisotropic elastic wave equations on parallel GPU devices. *Geophysics* **78**(2), 7–15 (2013). <https://doi.org/10.1190/geo2012-0063.1>

Publisher's Note Springer Nature remains neutral with regard to jurisdictional claims in published maps and institutional affiliations.